Magnetism of manganite nanotubes constituted by assembled nanoparticles

J. Curiale, R. D. Sánchez,*,† H. E. Troiani,† C. A. Ramos, and H. Pastoriza†
Centro Atómico Bariloche (CNyN), Comisión Nacional de Energía Atómica and Instituto Balseiro, Universidad Nacional de Cuyo, 8400 San Carlos de Bariloche, Rio Negro, Argentina

A. G. Leyva‡ and P. Levy†
Centro Atómico Constituyentes (CNyN), Comisión Nacional de Energía Atómica, B1650KNA Buenos Aires, Argentina
(Received 7 July 2006; revised manuscript received 18 January 2007; published 11 June 2007)

We present a study on the magnetic properties of manganite ultrafine grains assembled in nanotubes of 800 nm of external diameter and 6–8 μm length. The study includes two homogeneous ferromagnetic compounds, $La_{0.67}Ca_{0.33}MnO_3$ and $La_{0.67}Sr_{0.33}MnO_3$, and one exhibiting ferromagnetic and charge-ordered phase coexistence, $La_{0.325}Pr_{0.300}Ca_{0.375}MnO_3$. From magnetic measurements, we conclude that the grains behave as single magnetic domains. Observations of dipolar interactions between magnetic grains are evidenced by isothermal remanent magnetization and direct current demagnetization experiments. These experiments suggest that the grain magnetic moments should be arranged in a fanning configuration at $H=0$. Also, a uniaxial shape anisotropy was observed on previously aligned ferromagnetic nanotubes by ferromagnetic-resonance experiences. In $La_{0.325}Pr_{0.300}Ca_{0.375}MnO_3$, we observe distinctive features related to its inhomogeneous character as compared with the ferromagnetic homogeneous nanotubes.

DOI: 10.1103/PhysRevB.75.224410 PACS number(s): 75.75.+a, 75.47.Lx, 75.50.Tt, 76.30.−v

I. INTRODUCTION

The colossal magnetoresistance (CMR) introduced ten years ago with the perovskite manganites $R_{1-x}B_xMnO_3$, where R is a rare earth and B some alkali earth, has been extensively studied due to their unusual magnetic and electronic properties. The average ionic radius of the crystallographic A perovskite site, which is occupied by R and B ions, is an important parameter to determine the Mn-O-Mn angles and consequently its value affects the magnetism and transport properties. For large ionic radii A and doping values around $x=0.33$, the perovskite is metallic and it presents a ferromagnetic character. Two well-studied archetypes are $La_{0.67}Sr_{0.33}MnO_3$ and $La_{0.67}Ca_{0.33}MnO_3$. In certain mixed-valence manganites, with different doping (x) and/or R ions, the appearance of phase separation (PS) has been invoked to explain the CMR. The PS is a spontaneous intrinsic coexistence of regions exhibiting differentiated long-range order.[1] In the past years, experimental evidences and new techniques have allowed a direct observation of the phase-separation phenomenon, by tunneling and electron microscopies.[2–4] In particular, for small ionic radius of A ions, one representative manganite with coexistence between ferromagnetic metallic (FM) and charge-ordered (CO) phases is $La_{0.325}Pr_{0.300}Ca_{0.375}MnO_3$.

An additional extrinsic magnetoresistance at low magnetic fields was observed in granular materials. This effect is considerably enhanced by the reduction of the grain size,[5] which has generated a great interest as good candidates for potential applications.[6] This extrinsic magnetoresistance has been intensively investigated.[5,7] On the other hand, in manganites where their bulk presents phase separation, the molar fraction ratio between the FM and antiferromagnetic with CO phases can be tuned by controlling the grain size.[8]

At the nanoscale, wires and tubes are being intensively studied due to their particular properties and emerging applications. The recent advances in chemical synthesis methods allow the preparation of inorganic tubular and wire structures of, for example, vanadium oxide,[9] and $LaNiO_3$.[10] On the other hand, this wide spread of nanostructured materials can present diverse properties as ferroelectricity,[11] spin polarized transport,[12] ferromagnetism,[13–16] or magnetoresistivity.[17–19] Complex-oxide-based nanotubes could be used for future nanoelectronic components,[20–23] transducers, or sensors.[24,25]

In previous works,[12,13] we have reported the synthesis and morphological and structural study of nanowires and nanotubes (NTs) of perovskite rare-earth manganese oxide. In this paper, we focus on three systems: $La_{0.67}Sr_{0.33}MnO_3$ (LSMO), $La_{0.67}Ca_{0.33}MnO_3$ (LCMO), and $La_{0.325}Pr_{0.300}Ca_{0.375}MnO_3$ (LPCMO) reporting their morphology and magnetic response. The LCMO and LSMO in bulk develop homogeneous ferromagnetic properties below 273 and 360 K, respectively,[26] while LPCMO in bulk becomes CO at 220 K and FM at approximately 200 K. In the 210–75 K temperature range, it displays a PS regime, i.e., an intrinsic coexistence of FM and CO regions, and below 75 K, the ferromagnetism is dominant.[27,28] All the studied NTs present 800 nm external diameter and their walls are constituted by assembled nanoparticles (NPs). The aim of the present work is to study the effect on the magnetic properties exerted by the nanotube geometry and the NP that form the tube walls. We also report distinctive features observed in the LPCMO system related to its phase coexistence.

II. EXPERIMENT

We prepared nitric solutions of the desired cation ratio by dissolution in pure water. The analytical reagents used, depending on the manganite compound, were $La(NO_3)_3\cdot 6H_2O$, $Ca(NO_3)_2\cdot 6H_2O$, $Sr(NO_3)_2\cdot 6H_2O$, $Pr(NO_3)_3\cdot 6H_2O$ and $Mn(NO_3)_2\cdot 6H_2O$, respectively. We used the pore-filling method and the strategy consisted in the combination of a

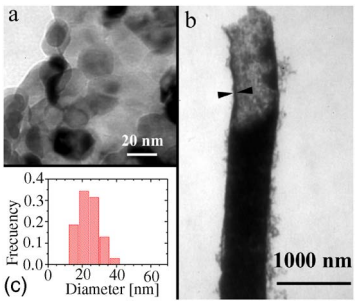

FIG. 1. (Color online) $La_{0.67}Sr_{0.33}MnO_3$ (LSMO). (a) Detail of the wall taken with the transmission electron microscope. (b) Isolated manganite nanotube with 700 nm of external diameter and a wall 45 nm wide. (c) Corresponding normalized histogram of the particle size distribution.

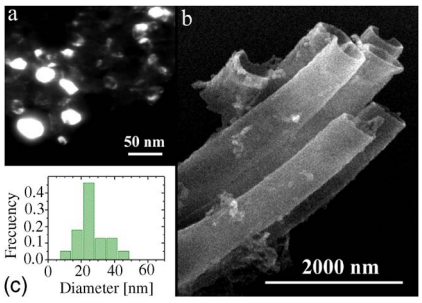

FIG. 2. (Color online) $La_{0.67}Ca_{0.33}MnO_3$ (LCMO). (a) Dark field TEM image of the wall detail of a single manganite tube nanostructure. (b) SEM image of a set of nanotubes. (c) Normalized histogram of the particle size distribution.

liquid precursor with a plastic template with nanochannels of approximately 800 nm diameter. Commercial porous polycarbonate films were filled with the solution in an adequate syringe filtration system. The reaction to obtain the desired compound proceeds by the denitration process of the confined precursor in a microwave oven. By adjusting the time and, therefore, the energy applied to the sample, it is possible to accomplish this reaction without producing damage to the polycarbonate film. The perovskite compounds are finally obtained, and the template is sacrificed during a thermal treatment in a standard furnace up to the final temperature of 1073 K.[12,13]

Transmission electron microscopy (TEM) was performed in a CM 200 Phillips microscope with an acceleration voltage of 200 kV, while the scanning electron microscopy (SEM) was performed in a Phillips XL30, both with a LaB_6 filament. Magnetization curves, between 4 and 300 K, were performed using a LakeShore 7300 series vibrating-sample magnetometer, with magnetic field (H) up to 10 kOe and a Quantum Design magnetic property measurement system (MPMS) superconduction quantum interference device (SQUID), with H up to 50 kOe. Ferromagnetic-resonance (FMR) spectra were taken in a Bruker ESP-300 spectrometer at room temperature.

III. RESULTS

A. Morphology

Each manganite nanotube is formed by an assembly of nanograins, as can be seen in the SEM and TEM micrographs in Figs. 1–3. Their typical length is ~6–8 μm. We also show the histograms of the characteristic grain diameter frequencies, which were computed from TEM micrographs. The most probable values are approximately 24, 28, and 35 nm for LSMO, LCMO, and LPCMO nanotubes, respectively. TEM reveals that the average wall thickness of the nanotubes is 45 nm, 60 nm, and 150 nm for LSMO, LCMO, and LPCMO, respectively. Dark field TEM experiments confirm that the crystalline orientation is random for all the nanotubes observed.

B. Magnetization and coercive field behavior

In this section, we compare the magnetic properties of the ferromagnetic NT (LSMO and LCMO) and the phase separated one (LPCMO). The magnetization T dependence was measured at different applied magnetic fields (we only show $H=100$ Oe in Fig. 4) following the next protocol: Zero-field cooling (ZFC) (1 in Fig. 4), cooling the sample from the highest T with $H=0$; afterward, a magnetic field of $H=100$ Oe was applied and the magnetization data were collected increasing T. Field cool cooling (FCC) (2 in Fig. 4) is performed by measuring the magnetization by cooling the sample with $H=100$ Oe. Finally, in field cool warming (FCW) (3 in the same plot), the system is warmed with $H=100$ Oe after FCC. Note the differences between the FCC (2^*) and FCW (3^*) curves in a broad T range for LPCMO-NT.

In the next paragraphs, we analyze the features of the initial magnetization and the hysteresis loops obtained from the different NTs studied. In Fig. 5, we show the magnetization for positive magnetic fields. The initial magnetization (M_i), or virgin magnetization curve, is the first M vs H run after cooling the sample down to 90 K with $H=0$. The figure also shows the subsequent M vs H runs defining the hysteresis loops. Note the LPCMO-NT case where M_i (labeled with *) is not easily saturated and it is outside the area defined by the hysteresis loop.

Differences between FCC and FCW curves (2^* and 3^* in Fig. 4) on one hand, and M_i values outside the subsequent hysteresis loops ("*" in Fig. 5), on the other hand, are features not observed in homogeneous FM nanotubes (without

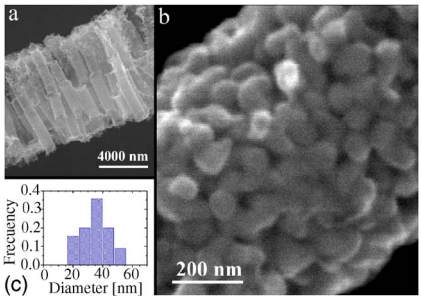

FIG. 3. (Color online) $La_{0.325}Pr_{0.300}Ca_{0.375}MnO_3$ (LPCMO). Scanning electron microscopy photographs of (a) set of aligned nanotubes immediately after synthesis. (b) Detail of the wall particle array in a single manganite nanotube. (c) The normalized histogram of the particle size distribution is shown.

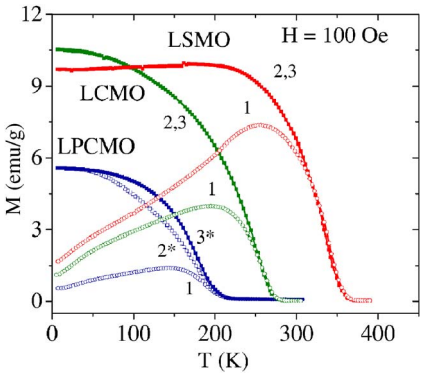

FIG. 4. (Color online) M vs T at 100 Oe of LSMO, LCMO, and LPCMO NTs after different magnetothermal processes. The numbers 1, 2, and 3 show the data collected in a (1) ZFC: warming process after cooling with zero magnetic field, (2) FCC: cooling process with a magnetic applied field of 100 Oe, and (3) FCW: warming after the FCC process with 100 Oe. The "*" indicates that the FCC and FCW in the LPCMO-NT are different.

phase separation) with similar dimensions and aspect ratio (as LSMO and LCMO NTs). For ferromagnetic materials, the critical diameter of a single magnetic domain can be estimated from[29–31]

$$D_s = \frac{9\sigma_\omega}{2\pi M_s^2}, \tag{1}$$

where $\sigma_\omega = 2\sqrt{AK}$ is the wall energy per unit area expressed in terms of the exchange stiffness constant (A) and the uniaxial anisotropy constant (K).

We estimated the value of A using a mean-field approximation.[29] In doing this, we used a Curie temperature (T_C) of 300 K, a lattice constant of 4 Å, and an average spin value $S=1.66$, $z=6$ for the number of nearest neighbors, yielding $A = 1.6 \times 10^{-6}$ erg/cm.

In the particular LSMO case,[32] the value of the magnetocrystalline anisotropy constant in single crystals is 1.8×10^4 erg/cm^3. From the observation of the TEM images (see, for instance, Figs. 1–3), we concluded that the grain aspect ratio is ≈ 1.5. A shape anisotropy for a prolate ellipsoid with this aspect ratio can be estimated as $K = 3.2 \times 10^5$ erg/cm^3,[35] which should be dominant in the total anisotropy value. The magnitude of K is consistent with the one that can be extracted from the FMR spectra, as will be mentioned later in Sec. III D.

Combining these values, and the theoretical saturation value at 0 K $M_s = 3.67 \mu_B/Mn$ (or $M_s \sim 91$ emu/g ~ 580 emu/cm^3), we obtain $D_s \approx 30$ nm. This result suggests that the grains of 20–30 nm, that constitute the nanotube walls are single magnetic domains (SMDs).

In all these NTs, the maximum M value reached is lower than the complete FM magnetization of the material. The saturation magnetization values reached are approximately half of the full expected ferromagnetic magnetization. This can easily be explained by invoking the presence of a magnetic dead layer (MDL) where the spins are practically paramagnetic, which are localized in the particle shell. The magnetic dead layer, in small particles, is a well-known phenomenon. Considering the nanoparticles constituting the wall of NT as perfectly spherical, we estimated the width of MDL for LSMO as 1.6 ± 0.4 nm. This is a reasonable value as compared with other small particles of oxides.[30,31,34]

On the other hand, the existence of a MDL at the grain boundaries is an essential factor to uncouple the magnetic moments. However, dipolar magnetic interactions could be a determinant factor to define the magnetic moment array at $H=0$. In the LPCMO-NT case, the difference between the magnetization for the bulk and the nanotubes cannot be directly associated with the MDL. Part of the magnetization reduction can be attributed to the PS nature of the compound. This is due to the fact that the CO phase inhibits the complete transformation of the material toward the FM phase and

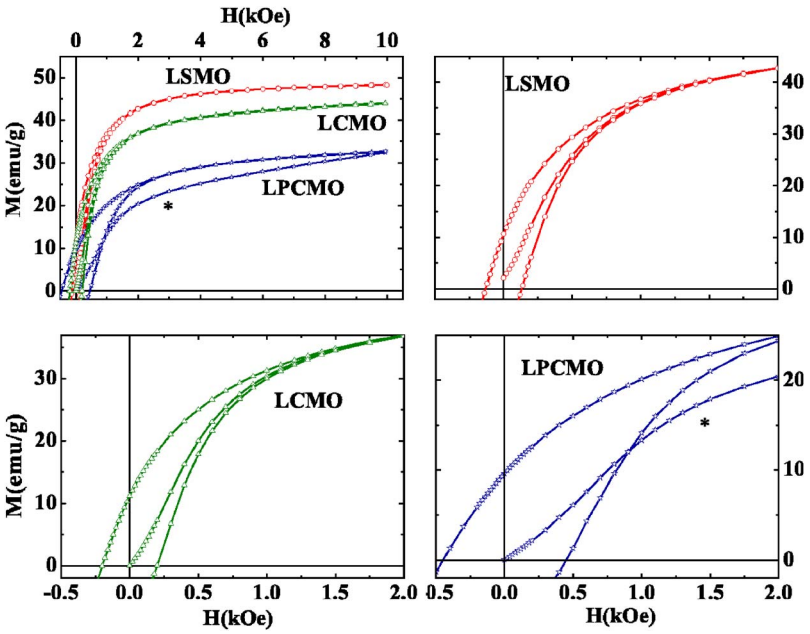

FIG. 5. (Color online) Detail of the hysteresis curves showing the initial magnetization (M_i) and magnetization (M) for LSMO (stars), LCMO (triangles), and LPCMO (circles) NTs at 90 K. The M_i curve out of the hysteresis loop area "*" is a distinctive feature of LPCMO-NT.

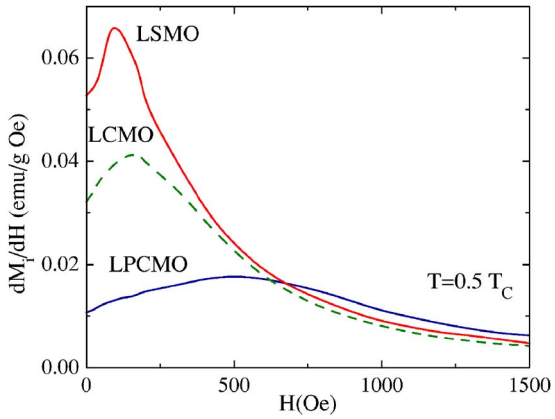

FIG. 6. (Color online) The dM_i/dH vs H at $T=0.5T_C$ of LPCMO, LCMO, and LSMO NTs.

as a consequence, we would expect a more complex interacting system.

In order to clarify these points, we analyzed the initial magnetization derivative with respect to the magnetic field. In Fig. 6, we compare the dM_i/dH at $T=0.5T_C$ for the different NTs studied and it is shown that the dM_i/dH maximum is located at a higher field for LPCMO-NT (550 Oe) than for LCMO and LSMO (200 and 100 Oe, respectively).

In Fig. 7, we plotted dM_i/dH vs H at different temperatures for LPCMO-NT. The curve at 90 K presents a maximum value, which is shifted to lower H when T is increased and this maximum disappears at approximately 180 K. As can be seen in the inset of Fig. 7, the temperature dependence of the magnetic susceptibility at 10 kOe taken from the initial magnetization curves, $dM_i/dH=\chi_{10\ \mathrm{kOe}}(*)$, remains constant in the $80<T(\mathrm{K})<175$ interval. At the lowest temperature measured, the $\chi_{10\ \mathrm{kOe}}(*)$ value is two times larger than $dM/dH=\chi_{10\ \mathrm{kOe}}$ obtained from the subsequent magnetization runs. This second curve increases from low T up to near T_C like a standard ferromagnetic material. This

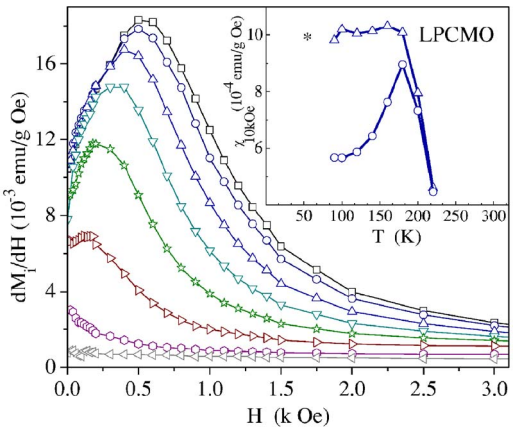

FIG. 7. (Color online) dM_i/dH vs H at different temperatures (90 K, open squares; 100, 120, 140, 160, 180, 200, and 220 K, curves) of LPCMO NT. Inset: T dependence of the high-field susceptibility, slope of M vs H at 10 kOe, in the virgin magnetization curve ("*")—this feature is only observed in LPCMO-NT—and slopes obtained from subsequent M vs H curves.

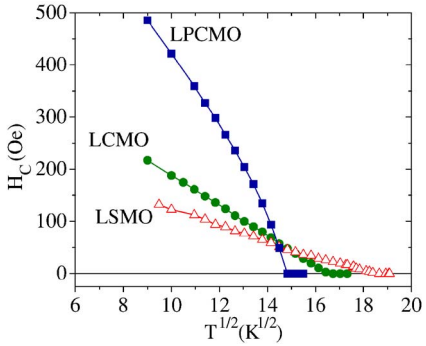

FIG. 8. (Color online) Square-root temperature dependence of the coercive field for the studied LPCMO, LCMO, and LSMO NTs.

fact stresses the difficulty to magnetize the sample from the virgin configuration state.

A major difference found in hysteresis loops, comparing the LPCMO-NT with the LPCMO bulk compound, is a nonnegligible coercive field (at 90 K, $H_C=414$ Oe and 50 Oe for NT and bulk, respectively). LCMO and LSMO NTs present lower H_C values but, in all cases, the observed values are higher than the corresponding bulk ones.[17] The coercive field follows a linear dependence with the square root of temperature for LCMO and LSMO NTs (see Fig. 8), but it is not linear for the LPCMO. Normally, a linear dependence is expected for noninteracting particle systems,[33] which can originate in the SMDs that constitute the walls of the ferromagnetic NT.

The maximum expected field for the reverse magnetic moments in LSMO-NT is the intrinsic coercivity $H_{Ci}=2K/M_s\sim 1100$ Oe, but the extrapolation of H_C at $T=0$ K is approximately 300 Oe. This reduction can be explained considering dipolar interactions between the SMDs, which adopt a fanning configuration at $H=0$ to minimize the magnetostatic energy ($H_{Ci}=\pi/6\ M_s\sim 300$ Oe).[33]

Thus, the distinctive features observed in LPCMO-NT below T_C are the virgin magnetization curve is outside of the subsequent hysteresis loops (and differences are found in $\chi_{10\ \mathrm{kOe}}$ upon cycling H), significant differences between the cooling/warming magnetization processes, and the coercive field values higher than the FM NT cases. These experimental facts can be associated with the competition between the charge-ordered and the ferromagnetic phases.

C. Magnetic interactions and activation volume in homogeneous ferromagnetic nanotubes

Based on findings described in Sec. III B about the phase coexistence regime developed in LPCMO, we focus this part of the study only on homogeneous ferromagnetic samples.

In order to identify the presence of the predominant magnetic interaction among particles, we measured the isothermal remanent magnetization (IRM) and the dc demagnetization (DCD) at different temperatures.[35,36] The IRM experiment starts with the sample totally demagnetized after cooling in the ZFC condition. The remanent magnetization is measured at $H=0$ after the application of different magnetic fields for 5 s. The applied fields were increased from $H=0$,

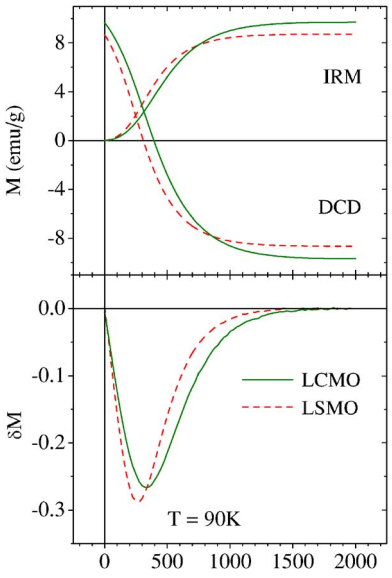

FIG. 9. (Color online) Top panel shows remanent magnetization as a function of the applied magnetic field (up to 2000 Oe) for 5 s in the IRM and DCD experiments, respectively. In the bottom panel, calculated δM values for the studied nanotubes are depicted.

with steps of 25 Oe, up to 2000 Oe (see IRM curves in the upper panel of Fig. 9 for the compositions studied at 90 K). The DCD experiment starts after cooling the sample in the ZFC condition to the target temperature. The sample is initially magnetized in the positive saturated state (in this case, it is reached by applying 2000 Oe). Then, a negative magnetic field is applied, which is turned off after 5 s and, finally, the remanent magnetization (M_{DCD}) is recorded at $H=0$. The negative applied field, after each positive saturated state, was increased from $H=0$ Oe, with steps of −25 Oe, up to −2000 Oe. It is important to remark that the difference between IRM and DCD experiments is essentially that one originates from a virgin state (IRM) and the other from the saturated state (DCD). In the upper panel of Fig. 9, IRM and DCD remanent magnetizations are plotted. Note that the sign of H for the DCD experiment was changed for an easy comparison. In a noninteracting system of particles with uniaxial anisotropy, it is expected that both IRM and DCD curves present the same values and therefore the Wohlfarth relation[37] is recovered ($1-2m_{IRM}=m_{DCD}$), where m is the normalized remanent magnetization with respect to the saturation values.

The presence of magnetic interactions in the system is manifested by the δM parameter,[38] which is defined by the following equation and it is zero in a magnetic noninteracting system

$$\delta M = m_{DCD} - (1 - 2m_{IRM}). \tag{2}$$

The comparison of the experimental δM values of the studied nanotubes is shown at the bottom panel of Fig. 9.

Negative δM values indicate that the dominant magnetic interactions are of dipolar type or that the sample is more easily demagnetized than magnetized. The magnetic field where δM is minimum is around 300 Oe, which gives an idea of the magnitude of the dipolar interactions. At high fields in the saturated state where the external magnetic field surpasses the dipolar interaction, both absolute values of M_{IRM} and M_{DCD} are equal and a zero value is expected for δM (see at high field in the lower panel of Fig. 9).

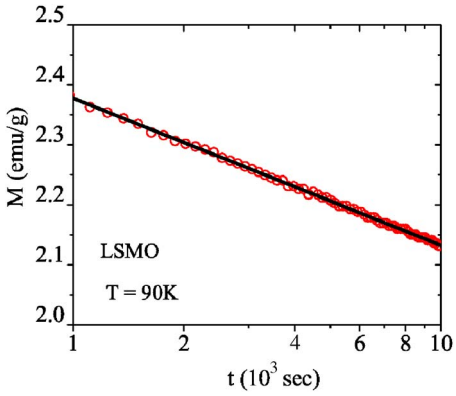

FIG. 10. (Color online) Relaxation data at 100 Oe for the LSMO-NT sample (open circles) and fit using Eq. (3) (line).

In what follows, we estimate for LSMO and LCMO ferromagnetic NTs the activation volume (v_{ac}). It is the SMD volume assuming a model with noninteracting particles. The first step to obtain v_{ac} is performed by measuring the magnetic viscosity, which is obtained from magnetic relaxation experiments. We saturated the magnetization of a sample in one direction; subsequently, we applied a steady reverse field in an opposite direction. The magnetization changes in time and a magnetic relaxation can be measured until the corresponding final magnetization is reached. This is a thermally activated process which can be described at fixed temperature by the equation[39]

$$M(t) = C + S \ln\left(\frac{t}{t_0}\right), \tag{3}$$

where t is the elapsed time since the opposite field was applied, and C and t_0 are constants. S is the magnetic viscosity which depends on temperature, saturation magnetization, and the distribution of activation energies.[40,41]

The powder of LSMO-NT was cooled to 90 K with an applied magnetic field of −10 kOe, then a field of 100 Oe was applied and the magnetization was measured as a function of time. Both the experimental magnetization data and the best fit with Eq. (3) are shown in Fig. 10 and, consequently, the magnetic viscosity coefficient (S) is calculated.

The second step is to obtain the irreversible susceptibility[40] (χ_{irr}) which depends on the dc demagnetization (M_{DCD}). It includes the irreversible contribution to the magnetization process[41] and the fluctuation field (H_f):[42]

$$\chi_{irr} = \frac{dM_{DCD}}{dH} = \frac{S}{H_f}. \tag{4}$$

The H_f, in Eq. (4), was introduced early by Néel[43] taking into account the thermal fluctuations and the activation volume

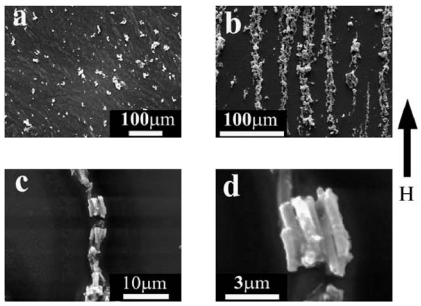

FIG. 11. Dispersed NT of LSMO: (a) at $H=0$ Oe, (b) under 1500 Oe applied magnetic field, and (c) and (d) are details of the chain order of LSMO-NT of the micrograph with $H=1500$ Oe. The H direction is represented by the arrow on the right of the images.

$$H_f = \frac{k_B T}{v_{ac} M_s}. \tag{5}$$

Taking both relations, we can write

$$\frac{dM_{DCD}}{dH} = \frac{S v_{ac} M_s}{k_B T}. \tag{6}$$

The final step is the estimation of v_{ac} using Eq. (6), which gives $v_{ac} \approx 1 \times 10^{-17}$ cm^3. This value corresponds to a hypothetical spherical particle with 26 ± 3 nm of diameter, which is in good agreement with the single-crystal micrograph of the particles that form the tube walls and also it confirms our previous estimation that these particles are single magnetic domains. For the LCMO-NT, and using the same procedure described above, we obtained the same activation volume value derived for the LSMO-NT case.

Furthermore, the dipolar interaction between the nanograins, and the agreement between the active volume and the single magnetic domain estimation reinforce the picture (described above) of weakly interacting magnetic moments for LSMO and LCMO nanotubes. In the next section, we try to elucidate the influence of the tube shape on the magnetism of these systems.

D. Ferromagnetic resonance in aligned nanotubes

In an attempt to determine directly a shape magnetic anisotropy associated with these hollow nanostructures, we prepared some samples with partially aligned nanotubes. We diluted powder of randomly oriented LSMO-NT in ethyl alcohol at room temperature, dispersed it on a glass substrate, and placed it on a magnetic field. When the solvent was completely evaporated, the resulting samples were studied in a SEM microscope. We observed random orientation of the ferromagnetic NT for $H < 300$ Oe. When $H > 500$ Oe, the NTs orient during the solvent evaporation process with their long axis along the direction of H. For a clear observation of this effect, we show in Fig. 11 the disordered and the aligned NT for $H=0$ and 1500 Oe, respectively. Also, the detail of the chain of the NT formed to minimize the magnetostatic energy is shown, which directly demonstrates that the easy axis of the NT develops along the tube's geometrical axis.

We performed a FMR experiment at room temperature and for different angles on these aligned NTs. In Fig. 12, we show two representative FMR spectra obtained measuring parallel ($\parallel$) and perpendicular ($\perp$) to the alignment direction. In this figure, we also indicate a peak-to-peak linewidth ($\Delta H_{PP} \approx 1.5$ kOe). If this asymmetric line is associated with a random distribution of anisotropy axes, ΔH_{PP} would give information of an average anisotropy constant of $K = MH_A/2$, where $\Delta H_{PP} \approx 2H_A/3$.[44] Thus, we obtain an average anisotropy constant of 2.9×10^5 erg/cm^3 which is close to the shape anisotropy value estimated previously from TEM images (see Sec. III B).

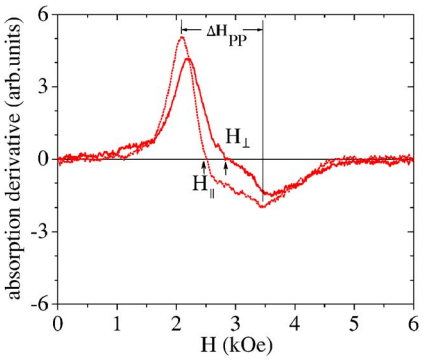

FIG. 12. (Color online) FMR of LSMO aligned NT at 9.4 GHz and room temperature. The dot line spectrum corresponds to the configuration with the field along the tube axis and the full line spectrum corresponds to the magnetic field perpendicular to the long tube axis.

The resonance field (H_{res}), taken as indicated in Fig. 12, is plotted for the range between 0° and 360° varying in steps of 10° (Fig. 13). The H_{res} curve shows a symmetry of 180° in agreement with the axial symmetry of the aligned nanotubes. For a system with this characteristics, we expect that the maximum H_{res} value corresponds to $H_\perp$ (hard direction) while the minimum must be associated with $H_\parallel$ configuration (easy direction).

In order to describe the angular variation, we write the free energy with an effective uniaxial magnetic anisotropy (K_{eff}) along the tube axis

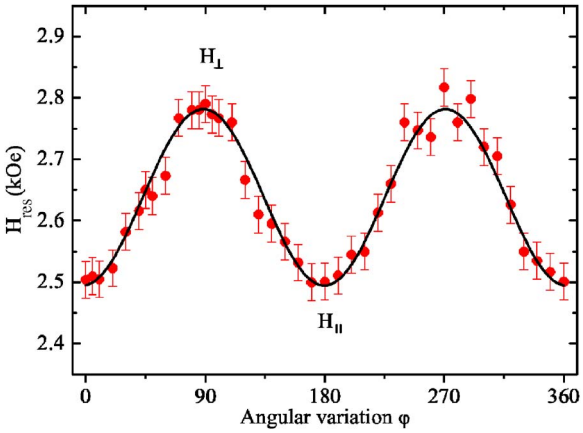

FIG. 13. (Color online) Angular variation of the resonance field of the ferromagnetic resonance of LSMO aligned NT. The lines are fits using Eq. (8) to describe the angular dependence.

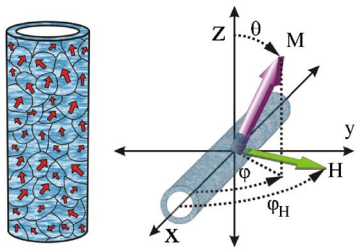

FIG. 14. (Color online) (a) Sketch of a fanninglike grain moment configuration at $H_{\parallel} \gtrsim H_C$. (b) Polar and azimuthal angles of M and H.

$$E = -K_{eff} \sin^2 \theta \cos^2 \varphi - \vec{\mathbf{M}} \cdot \vec{\mathbf{H}}. \quad (7)$$

The polar and azimuthal angles of the magnetization and the applied field are θ, θ_H, φ, and φ_H, respectively (see Fig. 14). Following the Smit and Beljers method,[45] in particular, for $\varphi = \varphi_H$ (which is fulfilled in low anisotropy materials), the frequency-field dispersion is

$$\frac{\omega}{\gamma} = [(H_{eff} \cos 2\varphi + H_{res})(H_{eff} \cos^2 \varphi + H_{res})]^{1/2}. \quad (8)$$

The angular variation of H_{res} can be well described with Eq. (8). The maximum field variation of approximately 300 Oe yields a value of $K_{eff} = 8 \times 10^4$ erg/cm^3, which is larger than the crystalline anisotropy measured in single crystals.[32] This enhancement could be explained by the presence of the tubular shape anisotropy. However, the calculated demagnetization field of circular cylinders (with the same aspect ratio as the present NT) in perpendicularly applied magnetic field[46] is close to $\approx 0.45(4\pi M_s) = 3280$ Oe. This value shows the limit of an ideal case where the NTs are completely isolated and the magnetization is not frustrated by the granular structure. Also, the interaction between the NT [see aggregates of NT in Figs. 11(d)] could play the role of diminishing the effective anisotropy of the system.

IV. DISCUSSION AND SUMMARY

The magnetic behavior of the ferromagnetic manganite nanotubes can be easily rationalized. The wall of the tubes is formed by magnetic nanograins. The size of the magnetic particles is less than the critical size for multidomain formation in manganites. As a consequence, each particle that constitutes the NT walls is a single magnetic domain. Indeed, this magnetic size was also corroborated by the magnetic activation volume which was estimated from the magnetic DCD and relaxation experiments. The low saturation magnetization suggests the existence of a magnetic dead layer, which avoids the propagation of the exchange interaction among the magnetic grains. The IRM and DCD magnetization experiments clearly demonstrate the demagnetizing tendency of the NT due to the dipolar contribution predominance. The magnitude of this was estimated in approximately 300 Oe.

Along the axis tube due to dipolar interactions, we expect a fanning configuration of the SMD magnetic moments at $H = 0$. Due to the important NT aspect ratio, the fanning ordering of the SMD moments introduces a small component along the axis tube, yielding a small shape anisotropy. The angular dependence of the FMR experiments on LSMO aligned ferromagnetic nanotubes also confirms the influence of the nanostructured shape.

For the system with phase separation (LPCMO), the coexistence of the CO and FM phases introduces an extra factor showing a complex magnetic behavior. The strain related to the small grain size can affect the hard CO phase generating paramagnetic regions with charge disorder (CD).[47] As a consequence, we expect the FM regions to be essentially SMD. A plausible picture is that when the sample is cooled with $H = 0$, SMDs coexist with CO/CD regions and the FM moments are randomly oriented minimizing the magnetostatic energy. Considering the TEM information (grain sizes around 35 nm) and the additional presence of a CO phase in this material, the size of the FM domains should be even more limited. Under an isothermal increase of H, the initial orientation of M within each grain is retained; yet, at larger H, the FM/CD boundaries can move transforming part of the CD into a FM region. But, as H cannot change all the CD/CO regions, a hard magnetization aspect to the M vs H curve is obtained (curve with * in Fig. 5 and inset of Fig. 7). This behavior suggests that during this displacement, the FM/CD wall should surmount some extra energy barrier when seeking for other more stable minima corresponding to larger FM volume fraction. The shift of the maximum value in dM_i/dH observed in LPCMO, with respect to the corresponding maximum of LCMO and LSMO, supports this idea, suggesting the presence of two mechanisms to magnetize the sample. The field is able to move the FM/CD-CO wall and consequently increase the SMD size. The SMD growth and the more ordered configuration obtained at large fields allow the FM zones to be closer and to interact more strongly. After this situation is reached, we would expect the coupling of moments in each tube, thus yielding a typical FM hysteresis loop (Fig. 5). The same picture can explain the M behavior for the FCC and FCW conditions (Fig. 4). The decrease of T (FCC) induces the increase of the SMD size in detriment of the CD zones, thus favoring the interaction between the moments. This more linked structure presents a M vs T shape reminding a mean-field-like behavior when the sample is warmed again (FCW).

In summary, this paper presents a magnetic study and a detailed comparison of properties of powders of randomly oriented $La_{0.67}Sr_{0.33}MnO_3$, $La_{0.67}Ca_{0.33}MnO_3$, and $La_{0.325}Pr_{0.300}Ca_{0.375}MnO_3$ nanotubes, which are formed by assembled nanoparticles.

$La_{0.67}Sr_{0.33}MnO_3$ and $La_{0.67}Ca_{0.33}MnO_3$ NTs present a homogeneous ferromagnetic behavior below 340 and 258 K, respectively. The magnetic dead layer avoids the exchange interaction between the nanograins, but the dipolar interaction between them was detected which suggests a fanning array of magnetic moments along the tube axis. The coercive field temperature dependence indicates the presence of weak interactions.

The $La_{0.325}Pr_{0.300}Ca_{0.375}MnO_3$ NT, as in the case of bulk samples, becomes mainly ferromagnetic below 200 K. The thermal hysteresis and the low magnetization values demon-

strate the presence of an extra charge-ordered phase. The small grain size may generate small charge-disordered regions, which are easily transformed to a ferromagnetic region by field or increasing/decreasing temperature. Also, the charge-disordered phase attenuates the interaction between single magnetic domains and when this phase is reduced by the application of a magnetic field, the system increases its ferromagnetic character. The control of the phase fraction could be used to tune the magnitude of the interaction between single magnetic domains which affects the coercive field and remanence. Finally, overall presented and discussed results contribute to the extensive magnetic characterization of these hollow nanostructures envisaged for spin-polarized transport.

ACKNOWLEDGMENTS

This work is part of a research project supported by Agencia Nacional de Promoción Científica y Tecnológica (Argentina) (PAV-Man and PICT under Grants No. 04-17-21372 and No. 03-13517, CONICET (Argentina) under Grant No. PIP 5250/05, and Fundación Antorchas and SECTyP-UNCuyo (Project No. 06/C203). The authors also thank J. Gómez and A. Butera for helpful discussions.

*Corresponding author. Electronic address: rodo@cab.cnea.gov.ar
†Also at Universidad Nacional de San Martín.
‡Also at CIC-CONICET.

[1] E. Dagotto, *Nanoscale Phase Separation and Colossal Magnetoresistance* (Springer, Germany, 2003); See also E. Dagotto, T. Hotta, and A. Moreo, Phys. Rep. **344**, 1 (2001), and references therein.
[2] M. Fäth, S. Freisem, A. A. Menovsky, Y. Tomioka, J. Aarts, and J. A. Mydosh, Science **285**, 1540 (1999).
[3] M. Uehara, S. Mori, C. H. Chen, and S.-W. Cheong, Nature (London) **399**, 560 (1999).
[4] S. Mori, C. H. Chen, and S.-W. Cheong, Phys. Rev. Lett. **81**, 3972 (1998).
[5] R. D. Sánchez, J. Rivas, C. Vázquez-Vázquez, A. López-Quintela, M. T. Causa, M. Tovar, and S. Oseroff, Appl. Phys. Lett. **68**, 134 (1996).
[6] J. M. D. Coey, J. Appl. Phys. **85**, 5576 (1999).
[7] Ll. Balcells, J. Fontcuberta, B. Martínez, and X. Obradors, Phys. Rev. B **58**, R14697 (1998).
[8] P. Levy, F. Parisi, G. Polla, D. Vega, G. Leyva, H. Lanza, R. S. Freitas, and L. Ghivelder, Phys. Rev. B **62**, 6437 (2000).
[9] L. Krusin-Elbaum, D. M. Newns, H. Zeng, V. Derycke, J. Z. Sun, and R. Sandstrom, Nature (London) **431**, 672 (2004).
[10] M. Tagliazucchi, R. D. Sánchez, H. E. Troiani, and E. J. Calvo, Solid State Commun. **137**, 212 (2006).
[11] F. D. Morrison, Y. Luo, I. Szafraniak, V. Nagarajan, R. B. Wehrspohn, M. Steinhart, J. H. Wendorff, N. D. Zakharov, E. D. Mishina, K. A. Vorotilov, A. S. Sigov, S. Nakabayashi, M. Alexe, R. Ramesh, and J. F. Scott, Rev. Adv. Mater. Sci. **4**, 114 (2003).
[12] P. Levy, A. G. Leyva, H. Troiani, and R. D. Sánchez, Appl. Phys. Lett. **83**, 5247 (2003).
[13] A. G. Leyva, P. Stoliar, M. Rosenbusch, V. Lorenzo, P. Levy, C. Albonetti, M. Cavallini, F. Biscarini, H. E. Troiani, J. Curiale, and R. D. Sánchez, J. Solid State Chem. **177**, 3949 (2004).
[14] A. G. Leyva, P. Stoliar, M. Rosenbusch, P. Levy, J. Curiale, H. E. Troiani, and R. D. Sánchez, Physica B **354**, 158 (2004).
[15] J. Curiale, R. D. Sánchez, H. E. Troiani, H. Pastoriza, P. Levy, and A. G. Leyva, Physica B **354**, 98 (2004).
[16] Y. C. Sui, R. Skomski, K. D. Sorge, and D. J. Sellmyer, Appl. Phys. Lett. **84**, 1525 (2004).
[17] J. Curiale, R. D. Sánchez, H. E. Troiani, A. G. Leyva, and P. Levy, Appl. Phys. Lett. **87**, 043113 (2005).
[18] D. Zhu, H. Zhu, and Y. H. Zhang, J. Phys.: Condens. Matter **14**, L519 (2003).
[19] X. Ma, H. Zhang, J. Xu, J. Niu, and Q. Yang, Chem. Phys. Lett. **363**, 579 (2002).
[20] H. W. Ch. Postma, T. Teepen, Z. Yao, M. Grifoni, and C. Dekker, Science **293**, 76 (2001).
[21] S. A. Wolf, D. D. Awschalom, R. A. Buhrman, J. M. Daughton, S. Von Molnár, M. L. Roukes, A. Y. Chtchelkanova, and D. M. Treger, Science **294**, 1488 (2001).
[22] Greg Y. Tseng and James C. Ellenbogen, Science **294**, 1293 (2001).
[23] A. Bachtold, P. Hadley, T. Nakanishi, and C. Dekker, Science **294**, 1317 (2001).
[24] E. Comini, G. Faglia, G. Sberveglieri, Zhengwei Pan, and Zhong L. Wang, Appl. Phys. Lett. **81**, 1869 (2002).
[25] L. Hueso and N. D. Mathur, Nature (London) **427**, 303 (2004).
[26] S.-W. Cheong and H. Y. Hwang, in *Colossal Magnetoresistance Oxides*, Monographs in Condensed Matter Science, edited by Y. Tokura (Gordon and Breach, London, 1999), Chap. 7.
[27] M. Quintero, A. G. Leyva, P. Levy, F. Parisi, O. Agüero, I. Torriani, M. G. das Virgens, and L. Ghivelder, Physica B **354**, 63 (2004).
[28] N. D. Mathur and P. B. Littlewood, Phys. Today **56**(1), 25 (2003).
[29] C. Kittel, Rev. Mod. Phys. **21**, 541 (1949).
[30] R. D. Sánchez, D. Caeiro, M. Östlund, M. Servin, C. Vázquez-Vázquez, M. T. Causa, M. A. López-Quintela, J. Rivas, and S. Oseroff, Mater. Sci. Forum **235–238**, 831 (1997).
[31] R. D. Sánchez, J. Rivas, P. Vaqueiro, M. A. López-Quintela, and D. Caeiro, J. Magn. Magn. Mater. **247**, 92 (2002).
[32] Y. Suzuki, H. Hwang, S.-W. Cheong, T. Siegrist, R. van Dover, A. Asamitsu, and Y. Tokura, J. Appl. Phys. **83**, 7064 (1998).
[33] B. D. Cullity, *Introduction to Magnetic Materials* (Addison-Wesley, Reading, MA, 1972).
[34] M. A. López-Quintela, L. E. Hueso, J. Rivas, and F. Rivadulla, Nanotechnology **14**, 212 (2003).
[35] A. Butera, J. L. Westone, and J. A. Barnard, J. Appl. Phys. **81**, 7432 (1997).
[36] J. García-Otero, M. Porto, and J. Rivas, J. Appl. Phys. **87**, 7376 (2000).
[37] E. P. Wohlfarth, J. Appl. Phys. **29**, 595 (1958).
[38] Xiao-Dong Che and H. Neal Bertram, J. Magn. Magn. Mater. **116**, 121 (1992).
[39] R. Street and J. C. Wooley, Proc. Phys. Soc., London, Sect. A **62**,

562 (1949).
[40] R. Street, J. C. Wooley, and P. B. Smith, Proc. Phys. Soc., London, Sect. A **65**, 679 (1952).
[41] P. Gaunt, Philos. Mag. **34**, 775 (1976).
[42] E. P. Wohlfarth, J. Phys. F: Met. Phys. **14**, L155 (1984).
[43] L. Nèel, J. Phys. Radium **12**, 339 (1951).
[44] E. de Biasi, C. A. Ramos, and R. D. Zysler, J. Magn. Magn. Mater. **262**, 235 (2003).
[45] J. Smit and H. G. Beljers, Philips Res. Rep. **10**, 113 (1955).
[46] M. Kobayashi, Y. Ishikawa, and S. Kato, IEEE Trans. Magn. **32**, 254 (1996).
[47] V. Podzorov, B. G. Kim, V. Kiryukhin, M. E. Gershenson, and S.-W. Cheong, Phys. Rev. B **64**, 140406(R) (2001).